

See discussions, stats, and author profiles for this publication at: <https://www.researchgate.net/publication/337803396>

# Computing ill-posed time-reversed 2D Navier–Stokes equations, using a stabilized explicit finite difference scheme marching backward in time

Article in *Inverse Problems in Science and Engineering* · December 2019

DOI: 10.1080/17415977.2019.1698564

---

CITATIONS

0

READS

36

1 author:



Alfred Carasso

National Institute of Standards and Technology

66 PUBLICATIONS 1,100 CITATIONS

SEE PROFILE

# COMPUTING ILL-POSED TIME-REVERSED 2D NAVIER-STOKES EQUATIONS, USING A STABILIZED EXPLICIT FINITE DIFFERENCE SCHEME MARCHING BACKWARD IN TIME

ALFRED S. CARASSO\*

**Abstract.** This paper constructs an unconditionally stable explicit finite difference scheme, marching backward in time, that can solve an interesting but limited class of ill-posed, time-reversed, 2D incompressible Navier-Stokes initial value problems. Stability is achieved by applying a compensating smoothing operator at each time step to quench the instability. This leads to a distortion away from the true solution. However, in many interesting cases, the cumulative error is sufficiently small to allow for useful results. Effective smoothing operators based on  $(-\Delta)^p$ , with real  $p > 2$ , can be efficiently synthesized using FFT algorithms. Similar stabilizing techniques were successfully applied in other ill-posed evolution equations. The analysis of numerical stability is restricted to a related linear problem. However, extensive numerical experiments indicate that such linear stability results remain valid when the explicit scheme is applied to a significant class of time-reversed nonlinear 2D Navier-Stokes initial value problems.

Several reconstruction examples are included, based on the *stream function-vorticity* formulation, and focusing on  $256 \times 256$  pixel images of recognizable objects. Such images, associated with non-smooth underlying intensity data, are used to create severely distorted data at time  $T > 0$ . Successful backward recovery is shown to be possible at parameter values exceeding expectations.

**Key words.** 2D Navier-Stokes equations backward in time. High Reynolds numbers. Stabilized explicit marching difference scheme. Numerical experiments.

**AMS subject classifications.** 35Q30, 35R25, 65M12, 65M30.

**1. Introduction.** Significant applications in science and engineering have generated considerable interest in the development of effective computational techniques for solving ill-posed time-reversed evolution equations. In Environmental Forensics, much success has been achieved using backward parabolic equations to locate sources of both groundwater and atmospheric contaminant plumes [1–3]. In Geophysics, the inverse problem of thermal evolution of the Earth interior is of major interest [4, 5]. In Image Science, time-reversed fractional and logarithmic diffusion equations have been successfully applied to deblur nanoscale scanning electron micrographs, as well as galactic scale Hubble space telescope imagery [6–8]. In Aerodynamics, backward Burgers’ equations play a central role in questions of inverse design associated with minimizing aircraft sonic boom [9–11]. Backward Burgers’ equations are also of prime interest in data assimilation studies in Geophysical Fluid Dynamics [12, 13].

Continuing the line of work developed in [14–19], the present self-contained paper constructs an unconditionally stable explicit finite difference scheme, marching backward in time, that can solve an interesting but limited class of ill-posed time-reversed 2D incompressible Navier-Stokes initial value problems. Stability is achieved by applying a compensating smoothing operator at each time step to quench the instability. Eventually, this leads to a distortion away from the true solution. However, in many interesting cases, the cumulative effect of these errors is sufficiently small to allow for useful results. Effective smoothing operators based on  $(-\Delta)^p$ , with real  $p > 2$ , can be efficiently synthesized using FFT algorithms. Similar stabilizing techniques were successfully applied in various other ill-posed equations, [14–19]. As was the case in these papers, the analysis of numerical stability given in Sections 5 and 6 below,

---

\*Applied and Computational Mathematics Division, National Institute of Standards and Technology, Gaithersburg, MD 20899. (alfred.carasso@nist.gov).

is restricted to a related linear problem. However, extensive numerical experiments indicate that these linear stability results remain valid when the explicit scheme is applied to a significant class of nonlinear problems.

Indeed, in the documented experiments discussed in Section 7, it is noteworthy that notwithstanding its limitations, the stabilized explicit scheme can produce useful reconstructions at parameter values far exceeding what would seem feasible, based on well-known uncertainty estimates for backward in time Navier-Stokes solutions.

In recent years, important new discretization methods have been developed for solving forward 2D incompressible Navier-Stokes equations, as well as other dissipative problems. See e.g., [20–28] and the references therein. Provided appropriate stabilizing operators can be constructed and applied at every time step  $t_n = n\Delta t$ , several such methods may possibly be marched backward in time, and produce valuable new computational tools for solving ill-posed time-reversed evolution equations.

**2. 2D Navier-Stokes equations.** Let  $\Omega$  be the unit square in  $R^2$  with boundary  $\partial\Omega$ . Let  $\langle \cdot, \cdot \rangle$  and  $\|\cdot\|_2$ , respectively denote the scalar product and norm on  $\mathcal{L}^2(\Omega)$ . We shall study the 2D problem in *stream function-vorticity* formulation [20, 21]. Here, the flow is governed by a stream function  $\psi(x, y, t)$  which defines the velocity components  $u(x, y, t) \equiv \psi_y$ ,  $v(x, y, t) \equiv -\psi_x$ , together with the vorticity  $\omega(x, y, t) \equiv v_x - u_y = -\Delta\psi$ . In this exploratory initial paper, we restrict attention to stream functions  $\psi$  defined on the unit square  $\Omega$ , which, for the limited duration  $0 \leq t \leq T$ , of the flow, *vanish* together with all their derivatives *near the boundary*  $\partial\Omega$ . However,  $\psi(x, y, t)$  will generally have large spatial derivatives away from the boundary. Given such a  $\psi(x, y, 0)$  and a kinematic viscosity  $\nu > 0$ , the *forward* Navier-Stokes initial value problem takes the form

$$\begin{aligned} \omega_t + u\omega_x + v\omega_y - \nu\Delta\omega &= 0, & \Delta\psi &= -\omega, & (x, y, t) &\in \Omega \times (0, T], \\ u(x, y, 0) &= \psi_y, & v(x, y, 0) &= -\psi_x, & \omega(x, y, 0) &= -\Delta\psi, \\ u(x, y, t) &= v(x, y, t) = \omega(x, y, t) = 0, & & & (x, y, t) &\in \partial\Omega \times [0, T]. \end{aligned} \tag{2.1}$$

Solving the system in Eq. (2.1) may be visualized as a marching computation as follows. Given the initial values, the evolution equation for  $\omega$  allows advancing  $\omega$  forward one time step  $\Delta t > 0$ . The Poisson equation  $\Delta\psi = -\omega$  is then solved to obtain  $\psi(x, y, \Delta t)$ , which leads to  $u(x, y, \Delta t)$ ,  $v(x, y, \Delta t)$ . This now allows advancing  $\omega$  to the next time step through the evolution equation, and so on.

With  $A$  the area of the flow domain, define  $U_{max}$  and the Reynolds number  $RE$  as follows

$$\begin{aligned} U_{max} &= \sup_{\Omega} \{u^2(x, y, 0) + v^2(x, y, 0)\}^{1/2}, \\ RE &= (\sqrt{A}/\nu)U_{max}. \end{aligned} \tag{2.2}$$

As in [14–19], our numerical experiments will involve  $256 \times 256$  pixel gray scale images. These images, defined by highly non-smooth underlying intensity data, present significant challenges to any ill-posed reconstruction algorithm. At the same time, using images of recognizable objects is highly instructive, as it enables immediate visual appreciation of the amount of distortion produced by the forward evolution, together with the subsequent partial undoing of that distortion by marching backward in time.

In [14–19], image intensity data were used directly to represent actual primary variables such as displacement, velocity, temperature, etc. In the present paper, image data are used to construct non-smooth stream functions  $\psi(x, y)$ , and the primary variables  $u$ ,  $v$ ,  $\omega$ , in Eq. (2.1) are derived by taking first and second *derivatives* of  $\psi$ . In particular, larger values of the Reynolds number  $RE$  are to be expected.

**3. Feasibility of backward in time Navier-Stokes reconstruction.** In dissipative evolution equations, there is a necessary uncertainty in backward in time reconstructions from imprecise data given at some positive time  $T$ . That uncertainty is a function of how quickly the given evolution equation forgets the past as time advances. This is a deep subject, explored in such publications as [30–38], and the references therein.

We now contemplate the feasibility of solving the system in Eq. (2.1), backward in time, from approximately known values. Let  $\{\tilde{u}(x, y, t), \tilde{v}(x, y, t), \tilde{\omega}(x, y, t)\}$ , be the solution on  $\Omega \times [0, T]$  corresponding to approximate data  $\{\tilde{u}(\cdot, T), \tilde{v}(\cdot, T), \tilde{\omega}(\cdot, T)\}$ , at a given positive time  $T$ , and let  $\{u(x, y, t), v(x, y, t), \omega(x, y, t)\}$  be the unique solution associated with the true data  $\{u(\cdot, T), v(\cdot, T), \omega(\cdot, T)\}$  at time  $T$ . Define  $w(x, y, t)$  on  $\Omega \times [0, T]$ , and  $F(t)$  on  $[0, T]$ , as follows

$$(w(x, y, t))^2 = \{u(x, y, t) - \tilde{u}(x, y, t)\}^2 + \{v(x, y, t) - \tilde{v}(x, y, t)\}^2, \quad (3.1)$$

$$F(t) = \|w(\cdot, t)\|_2^2 = \int_{\Omega} (w(x, y, t))^2 dx dy.$$

For a given small  $\epsilon > 0$ , assume that  $|w(x, y, T)|$  is small enough that  $F(T) \leq \epsilon$ . What constraints must be placed on the solutions of Eq. (2.1) to ensure that  $F(t)$  will remain small for  $0 \leq t < T$ ? This is the backward stability problem for the Navier-Stokes equations in the  $\mathcal{L}^2(\Omega)$  norm. The best known results in this direction were obtained by Knops and Payne using logarithmic convexity arguments [32, 33, 35].

Let  $P, Q$ , be prescribed positive constants. A velocity field  $\{u(x, y, t), v(x, y, t)\}$  is said to belong to the class  $\mathcal{P}$  if

$$\sup_{(x,t) \in \Omega \times [0,T]} \{(u^2 + v^2)\} \leq P^2, \quad (3.2)$$

while it belongs to the class  $\mathcal{Q}$  if

$$\sup_{(x,t) \in \Omega \times [0,T]} \{(u^2 + v^2) + \omega^2 + (u_t^2 + v_t^2)\} \leq Q^2. \quad (3.3)$$

Define  $a, b, c, \mu(t), K$ , as follows,

$$\begin{aligned} a &= 2(P^2 + 1)/\nu, & b &= Q^2(1 + a/\nu), \\ c &= b/a, & \mu(t) &= (e^{at} - 1)/(e^{aT} - 1), & 0 \leq t \leq T, \\ K &\equiv K(P, Q, \nu, t, T) = \exp\{c(t - \mu(t)T)\}, & 0 \leq t \leq T. \end{aligned} \quad (3.4)$$

If  $\{u(x, y, t), v(x, y, t)\} \in \mathcal{P}$  and  $\{\tilde{u}(x, y, t), \tilde{v}(x, y, t)\} \in \mathcal{Q}$ , it is shown in [32, 33] that then

$$F(t)F''(t) - (F'(t))^2 \geq aF(t)F'(t) - bF^2(t), \quad (3.5)$$

## JOAN CRAWFORD STREAM FUNCTION DATA

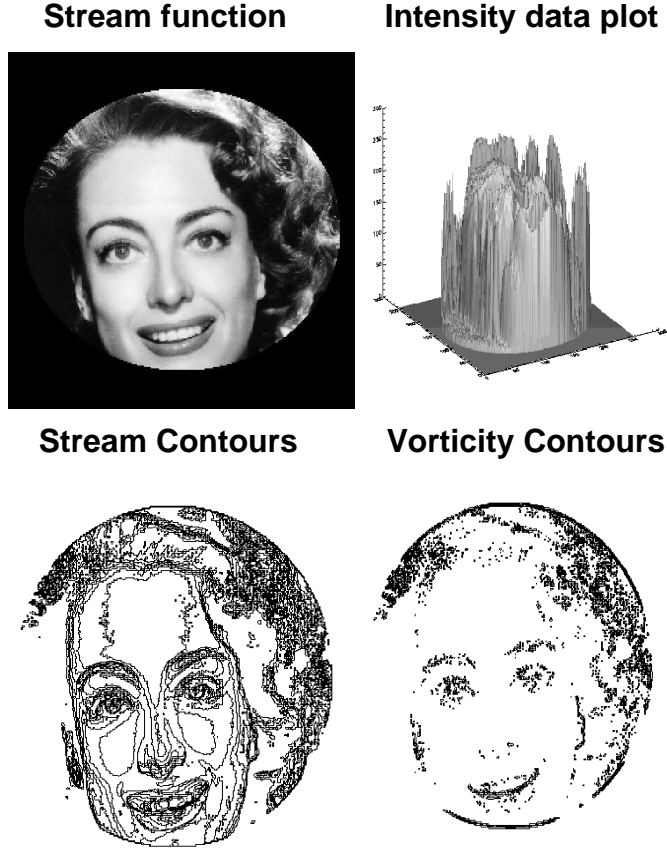


FIG. 3.1. *Non-smooth Joan Crawford data leads to challenging ill-posed Navier-Stokes reconstruction problem. Here,  $U_{max} = 114$ ,  $RE = 11400$ ,  $\sup_{\Omega}\{|\omega(x, y, 0)|\} = 1.0 \times 10^5$ . Theoretical uncertainty estimates indicate backward recovery of above data from distorted values at  $T > 0$ , would be feasible provided  $T \leq 1.0 \times 10^{-9}$ .*

from which, as will be shown below, it follows that

$$F(t) \leq e^{\{c(t-\mu(t)T)\}} \{F(0)\}^{1-\mu(t)} \{F(T)\}^{\mu(t)}, \quad 0 \leq t \leq T. \quad (3.6)$$

With  $\log x$  denoting the natural logarithm of  $x > 0$ , we establish Eq. (3.6) by reproducing the convexity arguments developed in [30, p. 18] and [31, p. 34]. We may assume that  $F(t) > 0$ ,  $0 \leq t \leq T$ , since, as was shown in [29], if  $F(t^\dagger) = 0$  for any  $t^\dagger$  in  $[0, T]$ , then  $F(t) \equiv 0$  on  $[0, T]$ , and Eq. (3.6) is trivially true in that case. Multiplying both sides of Eq. (3.5) by  $e^{-at}/F^2(t)$ , we find

$$(e^{-at}F'/F)' \geq -be^{-at}. \quad (3.7)$$

Let  $s = e^{at}$ , and change variables from  $t$  to  $s$  in Eq. (3.7). With  $G(s) = F(t)$ , we

then have  $F'(t) = (dG/ds)(ds/dt) = as(dG/ds)$ . Hence, from Eq. (3.7),

$$(e^{-at}F'/F)' = sa^2 d/ds\{(dG/ds)/G\} \geq -b/s. \quad (3.8)$$

Therefore, with  $s_1 = 1$ ,  $s_2 = e^{aT}$ ,

$$\begin{aligned} d^2/ds^2\{\log G(s)\} &\geq -b/(a^2s^2) = -d^2/ds^2\{\log(s^{-b/a^2})\}, & s_1 \leq s \leq s_2, \\ d^2/ds^2\{\log(G(s)s^{-b/a^2})\} &\geq 0, & s_1 \leq s \leq s_2. \end{aligned} \quad (3.9)$$

The last inequality implies that  $\log(G(s)s^{-b/a^2})$  is a convex function of  $s$  on  $[s_1, s_2]$ . Hence, on that same interval,

$$G(s)s^{-b/a^2} \leq \left\{G(s_1)s_1^{-b/a^2}\right\}^{(s_2-s)/(s_2-s_1)} \left\{G(s_2)s_2^{-b/a^2}\right\}^{(s-s_1)/(s_2-s_1)}. \quad (3.10)$$

Returning to the original  $t$  variable, Eq. (3.10) translates into Eq. (3.6). QED.

Next, in Eq. (3.1), let  $M$  be an a-priori bound for  $F(0) = \|w(\cdot, 0)\|_2^2$ . With  $F(T) \leq \epsilon$ , we then obtain from Eq. (3.6)

$$\|w(\cdot, t)\|_2^2 = F(t) \leq e^{\{c(t-\mu(t)T)\}} M^{1-\mu(t)} \epsilon^{\mu(t)}, \quad 0 \leq t \leq T. \quad (3.11)$$

However, as the example below indicates, even with small  $\epsilon > 0$ ,  $\|w(\cdot, t)\|_2$  need not be small for  $t < T$ , because the factor  $K = \exp\{c(t - \mu(t)T)\}$  may be extremely large, unless  $T$  is extremely small.

**3.1. An example: the Joan Crawford stream function.** The  $256 \times 256$  pixel gray-scale Joan Crawford image, shown in Figure 3.1, is defined by highly non smooth intensity data, with integer values ranging between 0 and 255. Here, these values are multiplied by 0.0025 to create an array  $\psi(x, y)$  of non negative numbers ranging from 0 to 0.6375. We now consider  $\psi(x, y)$  as a candidate initial stream function, defined on the unit square  $\Omega$ . Contour plots of  $\psi(x, y, 0)$  and of the associated vorticity  $\omega(x, y, 0) = -\Delta\psi$ , are also shown in Figure 3.1. However, even though  $0 \leq \psi(x, y, 0) \leq 0.6375$ , one must expect large values for its derivatives. Indeed, with  $U_{max}$  as in Eq. (2.2), we find

$$U_{max} \approx 114, \quad \sup_{\Omega}\{|\omega(x, y, 0)|\} \approx 1.0 \times 10^5. \quad (3.12)$$

Using  $\psi(x, y, 0)$  in Figure 3.1 together with  $\nu = 0.01$  in the forward problem in Eq. (2.1), and using  $A = 1$  in Eq. (2.2), leads to a Reynolds number  $RE \approx 11400$ . Without the above rescaling, these critical values would be 400 times larger.

We now assess the feasibility of reconstructing the initial values shown in Figure 1, from the data at time  $T$ . From Eqs. (3.2, 3.3, 3.4), we have

$$\begin{aligned} P^2 &> U_{max}^2 \approx 13000, & Q^2 &> 1.0 \times 10^{10}, \\ a &\approx 2.6 \times 10^6, & b &\approx 2.6 \times 10^{18}, & c &\approx 1.0 \times 10^{12}, \\ \mu(t) &= (e^{at} - 1)/(e^{aT} - 1), & K &= e^{\{c(t-\mu(t)T)\}}. \end{aligned} \quad (3.13)$$

With  $T = 1.0 \times 10^{-9}$ , and  $t = T/2$ , we find  $\mu(T/2) = 0.499675$ , and  $K \approx 1.4$ . However, with  $T = 1.0 \times 10^{-8}$ , and  $t = T/2$ , we now find  $\mu(T/2) = 0.49675$ , and  $K \approx 1.3 \times 10^{14}$ . Thus, if  $T \geq 1.0 \times 10^{-8}$ , the reconstruction uncertainty at  $t = T/2$ , given in Eq. (3.11), is much too large for any realistic value of the data error  $\epsilon$  at time  $T$ .

Rigorous uncertainty estimates, such as the Knops-Payne result in Eq. (3.11), must necessarily reflect worse-case error propagation scenarios, and may be too pessimistic in some cases. In Section 7 below, several backward recovery experiments are discussed and documented. In these experiments, the kinematic viscosity  $\nu = 0.01$ , and the associated Reynolds numbers  $RE$ , vorticities  $|\omega|$ , and speeds  $U_{max}$ , are of magnitudes comparable to those found in the Joan Crawford stream function in Figure 3.1, resulting in parameter values very similar to those displayed in Eqs. (3.12) and (3.13). Nevertheless, using the stabilized explicit scheme discussed in Eq. (4.8) below, remarkably good recovery at  $t = 0$  is found possible from approximate data at values of  $T$  on the order of  $1.0 \times 10^{-3}$ . However, at larger values of  $T$ , the resulting image blur becomes too severe and precludes useful reconstruction.

**4. Stabilized explicit schemes for the 2D Navier-Stokes Equations.** For well-posed initial value problems, explicit stepwise marching schemes are quite useful, but often require restrictive Courant stability conditions. Some explicit schemes, such as Richardson's leapfrog scheme, are unconditionally unstable for parabolic problems, [39, p. 190]. For ill-posed initial value problems, all consistent stepwise marching schemes, whether explicit or implicit, are necessarily unconditionally unstable [39, p. 59]. It is an important fact that one can stabilize explicit marching schemes, and render them *unconditionally stable* marching forward or backward in time, but at the cost of making them slightly *inconsistent*.

Consider the following 2D Navier-Stokes system for  $(x, y) \in \Omega$ ,

$$\omega_t = L^\dagger \omega \equiv \nu \Delta \omega - u \omega_x - v \omega_y, \quad \Delta \psi = -\omega, \quad 0 < t \leq T, \quad (4.1)$$

together with homogeneous boundary conditions on  $\partial\Omega$ , and the initial values

$$u(x, y, 0) = u_0(x, y), \quad v(x, y, 0) = v_0(x, y), \quad \omega(x, y, 0) = \omega_0(x, y). \quad (4.2)$$

The well-posed forward initial value problem in Eq. (4.1) becomes ill-posed if the time direction is reversed, and one wishes to recover  $u(x, y, 0)$ ,  $v(x, y, 0)$ ,  $\omega(x, y, 0)$ , from given approximate values for  $u(x, y, T)$ ,  $v(x, y, T)$ ,  $\omega(x, y, T)$ . We contemplate such time-reversed computations by allowing for possible *negative* time steps  $\Delta t$  in the explicit time-marching finite difference scheme described below. With a given positive integer  $N$ , let  $|\Delta t| = T/(N + 1)$  be the time step magnitude, and let  $\tilde{u}^n(x, y) \equiv \tilde{u}(x, y, n\Delta t)$ ,  $n = 0, 1, \dots, N + 1$ , denote the intended approximation to  $u(x, y, n\Delta t)$ , and likewise for  $\tilde{v}^n(x, y)$ ,  $\tilde{\omega}^n(x, y)$ . It is helpful to consider Fourier series expansions for  $\tilde{\omega}^n(x, y)$ , on the unit square  $\Omega$ ,

$$\tilde{\omega}^n(x, y) = \sum_{j,k=-\infty}^{\infty} \tilde{\omega}_{j,k}^n \exp\{2\pi i(jx + ky)\}, \quad (4.3)$$

with Fourier coefficients  $\{\tilde{\omega}_{j,k}^n\}$  given by

$$\tilde{\omega}_{j,k}^n = \int_{\Omega} \tilde{\omega}^n(x, y) \exp\{-2\pi i(jx + ky)\} dx dy, \quad (4.4)$$

Since  $\omega$  satisfies Eq. (4.1),  $\Delta\omega$  exists and is continuous. Hence, the Fourier series in Eq. (4.3) is expected to be well-behaved. In the error analyses discussed below,  $\omega_{tt}$ ,  $\omega_{ttt}$ ,  $\omega_{tttt}$ , will be assumed to exist and be continuous. From Eq. (4.1), this implies that

$$\|(\nu\Delta)^m\omega\|_2 < \infty, \quad m = 1, 4, \quad 0 \leq t \leq T. \quad (4.5)$$

With given fixed  $\gamma > 0$  and real  $p$  with  $1 < p \leq 3$ , define  $\lambda_{j,k}$ ,  $\sigma_{j,k}$ , as follows

$$\lambda_{j,k} = 4\pi^2\nu(j^2 + k^2), \quad \sigma_{j,k} = \exp\{-2\gamma|\Delta t|\lambda_{j,k}^p\}. \quad (4.6)$$

For functions  $\tilde{\omega}^n(x, y)$  satisfying Eq. (4.5), define the linear operators  $P$  and  $S$  as follows

$$\begin{aligned} P\tilde{\omega}^n &= \sum_{j,k=-\infty}^{\infty} \lambda_{j,k}^p \tilde{\omega}_{j,k}^n \exp\{2\pi i(jx + ky)\}, \\ S\tilde{\omega}^n &= \sum_{j,k=-\infty}^{\infty} \sigma_{j,k} \tilde{\omega}_{j,k}^n \exp\{2\pi i(jx + ky)\}. \end{aligned} \quad (4.7)$$

As in [14–19], the operator  $S$  is used as a stabilizing smoothing operator at each time step. With the operator  $L^\dagger$  as in Eq (4.1), let  $L^\dagger\tilde{\omega}^n \equiv \nu\Delta\tilde{\omega}^n - \tilde{u}^n\tilde{\omega}_x^n - \tilde{v}^n\tilde{\omega}_y^n$ . Consider the following *explicit* time-marching difference scheme for the system in Eq (4.1), in which only the time variable is discretized, while the space variables remain continuous,

$$\tilde{\omega}^{n+1} = S\tilde{\omega}^n + \Delta t S(L^\dagger\tilde{\omega}^n), \quad \Delta\tilde{\psi}^{n+1} = -\tilde{\omega}^{n+1}. \quad (4.8)$$

As already noted, we allow for negative time steps  $\Delta t$  in Eq. (4.8). The above semi-discrete problem is highly nonlinear. In the operator  $L^\dagger$ , the coefficients  $\tilde{u}^n = \tilde{\psi}_y^n$ ,  $\tilde{v}^n = -\tilde{\psi}_x^n$ , are defined in terms of  $\tilde{\omega}^n$ , which is needed to obtain  $\tilde{\psi}^n$  by solving the Poisson problem  $\Delta\tilde{\psi}^n = -\tilde{\omega}^n$ . The analysis presented in Sections 5 and 6 below, is relevant to the above semi-discrete problem. The Lemmas and Theorems presented in these two sections are results previously obtained in [19], in connection with 2D Burgers' equation. They are reproduced here and adapted to 2D Navier-Stokes equations for the convenience of the reader. In Section 7, where actual numerical computations are discussed, the space variables are also discretized, and FFT algorithms are used to synthesize the smoothing operator  $S$ .

**5. Fourier stability analysis in linearized problem.** As in [19], useful insight into the behavior of the nonlinear scheme in Eq. (4.8), can be gained by analyzing a related linear problem with constant coefficients. From a naive computational perspective, we may view  $L^\dagger$  in Eq. (4.1), as a linear operator with time-dependent coefficients  $u(x, y, t)$ ,  $v(x, y, t)$ , which need to be evaluated at every time step  $t = n\Delta t$ , through an independent subsidiary calculation. If  $|u(x, y, t)| \leq a$ ,  $|v(x, y, t)| \leq b$ , with positive constants  $a$ ,  $b$ , the numerical stability of the evolution equation  $\tilde{\omega}^{n+1} = S\tilde{\omega}^n + \Delta t S(L^\dagger\tilde{\omega}^n)$  in Eq. (4.8), may be investigated by considering the constant coefficient linear operator  $L\tilde{\omega}^n \equiv \nu\Delta\tilde{\omega}^n - a\tilde{\omega}_x^n - b\tilde{\omega}_y^n$ , in lieu of  $L^\dagger\tilde{\omega}^n$ . Accordingly, we examine the following evolution equation

$$\begin{aligned} \omega_t &= Lu \equiv \nu\Delta\omega - a\omega_x - b\omega_y, \quad 0 < t \leq T, \\ \omega(x, y, 0) &= \omega_0(x, y), \end{aligned} \quad (5.1)$$

together with periodic boundary conditions on  $\partial\Omega$ . Unlike the case in Eq. (4.8), the stabilized marching scheme

$$\tilde{\omega}^{n+1} = S\tilde{\omega}^n + \Delta tSL\tilde{\omega}^n, \quad n = 0, 1, \dots, N, \quad (5.2)$$

with the linear operator  $L$ , is susceptible to Fourier analysis. If  $L\tilde{\omega}^n = f^n(x, y)$ , then the Fourier coefficients  $\{f_{j,k}^n\}$  satisfy  $f_{j,k}^n = g_{j,k}\tilde{\omega}_{j,k}^n$ , where

$$g_{j,k} = -\{4\pi^2\nu(j^2 + k^2) + 2\pi i(aj + bk)\}. \quad (5.3)$$

Let  $R$  be the linear operator  $R = S + \Delta tSL$ . Then,

$$\begin{aligned} \tilde{\omega}^{n+1} &= R\tilde{\omega}^n = \sum_{j,k=-\infty}^{\infty} \tilde{\omega}_{j,k}^n \{1 + \Delta t g_{j,k}\} \sigma_{j,k}, \\ \|\tilde{\omega}^{n+1}\|_2^2 &= \|R\tilde{\omega}^n\|_2^2 \leq \sum_{j,k=-\infty}^{\infty} |\tilde{\omega}_{j,k}^n|^2 \{1 + |\Delta t| |g_{j,k}|\}^2 \sigma_{j,k}^2, \end{aligned} \quad (5.4)$$

on using Parseval's formula.

LEMMA 1. *Let  $\lambda_{j,k}$ ,  $\sigma_{j,k}$ , be as in Eq. (4.6), and let  $g_{j,k}$  be as in Eq. (5.3). Choose a positive integer  $J$  such that if  $\lambda_J = 4\pi^2\nu J$ , we have*

$$\max_{(j^2+k^2) \leq J} \{|g_{j,k}|\} \leq 2\lambda_J, \quad |g_{j,k}| \leq 2\lambda_{j,k}, \quad \forall (j^2 + k^2) > J. \quad (5.5)$$

With  $p > 1$ , choose  $\gamma \geq (\lambda_J)^{1-p}$  in Eq. (4.6). Then,

$$\sigma_{j,k} (1 + |\Delta t| |g_{j,k}|) \leq 1 + 2|\Delta t| \lambda_J. \quad (5.6)$$

Hence, from Eq. (5.4),

$$\begin{aligned} \|R\|_2 &\equiv \sup_{\{\omega \neq 0\}} \{\|R\tilde{\omega}^n\|_2 / \|\tilde{\omega}^n\|_2\} \leq 1 + 2|\Delta t| \lambda_J \leq \exp\{2|\Delta t| \lambda_J\}, \\ \|R^m\|_2 &\leq \|R\|_2^m \leq \exp\{2m|\Delta t| \lambda_J\}, \quad m \geq 1, \end{aligned} \quad (5.7)$$

and, for  $n = 1, 2, \dots, N + 1$ ,

$$\|\tilde{\omega}^n\|_2 = \|R^n \omega_0\|_2 \leq \exp\{2n|\Delta t| \lambda_J\} \|\omega_0\|_2. \quad (5.8)$$

Therefore, with this choice of  $(\gamma, p)$ , the explicit linear scheme in Eq. (5.2) is unconditionally stable, marching forward or backward in time.

*Proof:* We first show how to find a positive integer  $J$  such that Eq. (5.5) is valid. We have  $|g_{j,k}|^2 = \lambda_{j,k}^2 + 4\pi^2(aj + bk)^2 \leq \lambda_{j,k}^2 + (2c^2/\nu)\lambda_{j,k}$ , where  $0 < c = \max(a, b)$ . Choose a positive integer  $J$  such that  $\lambda_J = 4\pi^2\nu J > (2c^2/\nu)$ . Then,  $\forall (j, k)$ ,  $|g_{j,k}|^2 \leq \lambda_{j,k}^2 + \lambda_J \lambda_{j,k}$ , which implies Eq. (5.5). Next, the inequality in Eq. (5.6) is valid whenever  $(j^2 + k^2) \leq J$ , since  $\sigma_{j,k} \leq 1$ . For  $(j^2 + k^2) > J$ , we have  $\lambda_J < \lambda_{j,k}$  and  $|g_{j,k}| \leq 2\lambda_{j,k}$ . Hence

$$\sigma_{j,k} = \exp\{-2\gamma|\Delta t| \lambda_{j,k}^p\} \leq \exp\{-2\gamma|\Delta t| \lambda_{j,k} \lambda_J^{p-1}\} \leq \exp\{-2|\Delta t| \lambda_{j,k}\}, \quad (5.9)$$

since  $\gamma\lambda_J^{p-1} \geq 1$ . Also,  $\exp\{-2|\Delta t|\lambda_{j,k}\} \leq (1 + 2|\Delta t|\lambda_{j,k})^{-1}$ , since  $1 + x \leq e^x$  for real  $x$ . Hence, with  $|g_{j,k}| \leq 2\lambda_{j,k}$  for  $(j^2 + k^2) > J$ , we find  $\sigma_{j,k}(1 + |\Delta t||g_{j,k}|) \leq 1$ . Thus, Eq. (5.6) is valid  $\forall (j, k)$ . Next, using Eq. (5.6) in Eq. (5.4), together with Parseval's formula, leads to Eqs. (5.7) and (5.8). QED.

For functions  $h(x, y, t)$  on  $\Omega \times [0, T]$ , define the norm  $|||h|||_{2,\infty}$  as follows

$$|||h|||_{2,\infty} \equiv \sup_{0 \leq t \leq T} \{ \|h(\cdot, t)\|_2 \}. \quad (5.10)$$

LEMMA 2. Let  $\omega^n(x, y) \equiv \omega(x, y, n\Delta t)$ , assumed to satisfy Eq. (4.5), be the exact solution in Eq. (5.1). Let  $\gamma, p, \lambda_{j,k}, \sigma_{j,k}$ , be as in Eq. (4.6). Let  $P$  and  $S$  be as in Eq. (4.7), and let  $L$  be the linear operator in Eq. (5.1). Then,  $\omega^{n+1} = \omega^n + \Delta t L\omega^n + \tau^n$ , where  $\tau^n$  is the truncation error. With the norm definition in Eq (5.10), and  $0 \leq n \leq N$ ,

$$\begin{aligned} \|\tau^n\|_2 &\leq 1/2(\Delta t)^2 |||L^2\omega|||_{2,\infty}, \\ \|\omega^n - S\omega^n\|_2 &\leq 2\gamma|\Delta t| |||P\omega|||_{2,\infty}, \\ |\Delta t| \|L\omega^n - SL\omega^n\|_2 &\leq 2\gamma(\Delta t)^2 |||PL\omega|||_{2,\infty}. \end{aligned} \quad (5.11)$$

*Proof*: The inequality for the truncation error  $\tau^n$  in Eq. (5.11) follows naturally from a truncated Taylor series expansion. Since the linear operator  $L$  in Eq. (5.1) has constant coefficients, and  $\omega_t = L\omega$ , we have  $\omega_{tt} = L\omega_t = L^2\omega$ . Hence,

$$\begin{aligned} \omega^{n+1} &= \omega^n + \Delta t\omega_t^n + (1/2)(\Delta t)^2\omega_{tt}^n + O(\Delta t)^3, \\ \omega^{n+1} &= \omega^n + \Delta tL\omega^n + (1/2)(\Delta t)^2\overline{(L^2\omega)}, \end{aligned} \quad (5.12)$$

where  $\overline{(L^2\omega)}$  denotes the value of  $L^2\omega$  at an intermediate time  $t$ , lying between  $n\Delta t$  and  $(n+1)\Delta t$ . This proves the first inequality in Eq. (5.11). Using the inequality  $1 - e^{-x} \leq x$  for all real  $x$ , together with Parseval's formula, we have

$$\|\omega^n - S\omega^n\|_2^2 = \sum_{j,k=-\infty}^{\infty} |\omega_{j,k}^n|^2 (1 - \sigma_{j,k})^2 \leq (2\gamma|\Delta t|)^2 |||P\omega|||_{2,\infty}^2. \quad (5.13)$$

This proves the second inequality in Eq. (5.11). The last inequality is a corollary of the second. QED.

In Lemma 1, the finite difference approximation  $\tilde{\omega}^n(x, y) \equiv \tilde{\omega}(x, y, n\Delta t)$  satisfies Eq. (5.2), whereas the exact solution  $\omega^n(x, y) \equiv \omega(x, y, n\Delta t)$  in Eq. (5.1), satisfies  $\omega^{n+1} = \omega^n + \Delta t L\omega^n + \tau^n$ , where  $\tau^n$  is the truncation error. We need to estimate the error  $err^n(x, y) = \omega^n(x, y) - \tilde{\omega}^n(x, y)$ ,  $n = 0, 1, \dots, N+1$ .

THEOREM 1. With  $\Delta t > 0$ , let  $\omega^n(x, y)$ , assumed to satisfy Eq. (4.5), be the unique solution of Eq. (5.1) at  $t = n\Delta t$ . Let  $\tilde{\omega}^n(x, y)$  be the corresponding solution of the forward explicit scheme in Eq. (5.2), and let  $p, \lambda_J, \gamma$ , be as in Lemma 1. If  $err^n(x, y) = \omega^n(x, y) - \tilde{\omega}^n(x, y)$ , denotes the error at  $t = n\Delta t$ ,  $n = 1, 2, \dots, N+1$ , we have

$$\begin{aligned} \|err^n\|_2 &\leq e^{2t\lambda_J} \|err^0\|_2 + \{\gamma(e^{2t\lambda_J} - 1)/\lambda_J\} |||P\omega|||_{2,\infty} \\ &+ \{(e^{2t\lambda_J} - 1)/2\lambda_J\} \{2\gamma\Delta t |||PL\omega|||_{2,\infty} + (\Delta t/2) |||L^2\omega|||_{2,\infty}\}. \end{aligned} \quad (5.14)$$

*Proof:* Let  $h^n = \tau^n + (\omega^n - S\omega^n) + \Delta t(L\omega^n - SL\omega^n)$ . Let  $R$  be the linear operator in Eq. (5.4). Then,  $\omega^{n+1} = R\omega^n + h^n$ , while  $\tilde{\omega}^{n+1} = R\tilde{\omega}^n$ . Therefore

$$err^{n+1} = R\omega^n + h^n = R^{n+1}err^0 + \Delta t \sum_{j=0}^n R^{n-j} h^j / (\Delta t). \quad (5.15)$$

Let  $\|h\|_{2,\infty} \equiv \max_{0 \leq n \leq N+1} \{h^n\}$ . Using Eq. (5.7) in Lemma 1, and letting  $t = (n+1)\Delta t$ ,

$$\|err^{n+1}\|_{2 \leq} \leq e^{2t\lambda_J} \|err^0\|_{2 \leq} + \{\|h\|_{2,\infty} / \Delta t\} \Delta t \sum_{j=0}^n \|R^{n-j}\|_{2 \leq}. \quad (5.16)$$

We have  $\Delta t \sum_{j=0}^n \|R^{n-j}\|_{2 \leq} \leq \sum_{j=0}^n A_j$ , in Eq. (5.16), where, for each  $j$ ,  $A_j = \Delta t \exp\{2\lambda_J(n-j)\Delta t\}$ . Notice that with  $t = (n+1)\Delta t$ ,  $A_0$  is less than the area under the curve  $z(s) = \exp\{2\lambda_J(t-s)\}$  on the interval  $0 \leq s \leq \Delta t$ . Indeed,  $(\sum_{j=0}^n A_j)$  is less than the total area under that curve on the interval  $0 \leq s \leq t$ . Hence, from Eq. (5.16),

$$\begin{aligned} \|err^{n+1}\|_{2 \leq} &\leq e^{2t\lambda_J} \|err^0\|_{2 \leq} + \{\|h\|_{2,\infty} / \Delta t\} \int_0^t e^{2\lambda_J(t-s)} ds \\ &= e^{2t\lambda_J} \|err^0\|_{2 \leq} + \{\|h\|_{2,\infty} / \Delta t\} (e^{2t\lambda_J} - 1) / 2\lambda_J. \end{aligned} \quad (5.17)$$

Next, using Lemma 2 to estimate  $\{\|h\|_{2,\infty} / \Delta t\}$ , one obtains Eq. (5.14) from Eq. (5.17). QED.

**6. The stabilization penalties in the forward and backward linearized problem in Eq. (5.1).** The stabilizing smoothing operator  $S$  in the explicit scheme in Eq. (5.2) leads to unconditional stability, but at the cost of introducing a small error at each time step. We now assess the cumulative effect of that error.

In the forward problem in Theorem 1, we may assume the given initial data  $\omega_0(x, y)$  to be known with sufficiently high accuracy that one may set  $\|err^0\|_{2 \leq} = 0$  in Eq. (5.14). Choosing  $\gamma = (\lambda_J)^{1-p}$  in Lemma 1, and putting  $t = n\Delta t \leq T$ , Eq.(5.14) reduces to

$$\|err^n\|_{2 \leq} \leq (\lambda_J)^{-p} (e^{2t\lambda_J} - 1) \|P\omega\|_{2,\infty} + O(\Delta t), \quad n = 1, 2, \dots, N+1. \quad (6.1)$$

Therefore, when using the explicit scheme in Eq.(5.2), there remains the non-vanishing residual error  $(\lambda_J)^{-p} (e^{2t\lambda_J} - 1) \|P\omega\|_{2,\infty}$ , as  $\Delta t \downarrow 0$ . This is the *stabilization penalty*, which results from smoothing at each time step, and grows monotonically as  $t \uparrow T$ . Recall that  $\lambda_J$  must be chosen large enough to satisfy Eq. (5.5) in Lemma 1. Clearly, if  $T = (N+1)\Delta t$  is large, the accumulated distortion may become unacceptably large as  $t \uparrow T$ , and the stabilized explicit scheme is not useful in that case. On the other hand, if  $T$  is small, as is the case in problems involving small values of  $t$ , it may be possible to choose  $p > 2$  and sufficiently large  $\lambda_J$ , yet with small enough  $\lambda_J T$  that  $(\lambda_J)^{-p} (e^{2\lambda_J T} - 1)$  is quite small. In that case, the stabilization penalty remains acceptable on  $0 \leq t \leq T$ . As an example, with  $T = 2.0 \times 10^{-4}$ ,  $p = 3.25$ , and  $\lambda_J = 5.0 \times 10^4$ , we find  $(\lambda_J)^{-p} (e^{2\lambda_J T} - 1) < 2.6 \times 10^{-7}$ . This often leads to an acceptable  $\mathcal{L}^2$  relative error  $(\|err^n\|_{2 \leq} / \|\omega^n\|_{2 \leq})$ .

For this important but limited class of problems, the absence of restrictive Courant conditions on the time step  $\Delta t$  in the explicit scheme in Eq.(5.2), provides a significant advantage in well-posed forward computations of two dimensional problems on fine meshes.

However, there is an additional penalty in the ill-posed problem of marching backward from  $t = T$ , in that solutions exist only for a restricted class of data satisfying certain smoothness and other constraints. These data are seldom known with sufficient precision. We shall assume that the given data  $\tilde{\omega}^0(x, y)$  at  $t = T$ , differ from such unknown exact data by small errors  $\kappa(x, y)$ :

$$\tilde{\omega}^0(x, y) = \omega(x, y, T) + \kappa(x, y), \quad \|\kappa\|_2 \leq \epsilon. \quad (6.2)$$

**THEOREM 2.** *With  $\Delta t < 0$ , let  $\omega^n(x, y)$ , assumed to satisfy Eq. (4.5), be the unique solution of the forward well-posed problem in Eq. (5.1) at  $s = T - n|\Delta t|$ . Let  $\tilde{\omega}^n(x, y)$  be the corresponding solution of the backward explicit scheme in Eq. (5.2), with initial data  $\tilde{\omega}^0(x, y) = \omega(x, y, T) + \kappa(x, y)$  as in Eq. (6.2). Let  $p, \lambda_J, \gamma$ , be as in Lemma 1. If  $err^n(x, y) \equiv \omega^n(x, y) - \tilde{\omega}^n(x, y)$ , denotes the error at  $s = T - n|\Delta t|$ ,  $n = 0, 1, 2, \dots, N + 1$ , we have, with  $\epsilon$  as in Eq.(6.2),*

$$\begin{aligned} \|err^n\|_2 &\leq \epsilon e^{2n|\Delta t|\lambda_J} + (\gamma/\lambda_J) \left\{ (e^{2n|\Delta t|\lambda_J} - 1) \right\} \|P\omega\|_{2,\infty} \\ &+ \left\{ (e^{2n|\Delta t|\lambda_J} - 1)/\lambda_J \right\} \left\{ \gamma|\Delta t| \|PL\omega\|_{2,\infty} + (|\Delta t|/2) \|L^2\omega\|_{2,\infty} \right\}. \end{aligned} \quad (6.3)$$

*Proof:* Let  $h^n = \tau^n + (\omega^n - S\omega^n) + \Delta t(L\omega^n - SL\omega^n)$ . Let  $R$  be the linear operator in Eq. (5.4). Then,  $\omega^{n+1} = R\omega^n + h^n$ , while  $\tilde{\omega}^{n+1} = R\tilde{\omega}^n$ . Therefore

$$err^{n+1} = R err^n + h^n = R^{n+1}err^0 + |\Delta t| \sum_{j=0}^n R^{n-j} h^j / (|\Delta t|). \quad (6.4)$$

Let  $\|h\|_{2,\infty} \equiv \max_{0 \leq n \leq N+1} \{h^n\}$ . Using Lemma 1, and letting  $r = (n+1)|\Delta t|$ , we find, as in the case of Eq. (5.16),

$$\begin{aligned} \|err^{n+1}\|_2 &\leq \epsilon e^{2r\lambda_J} + \{\|h\|_{2,\infty}/|\Delta t|\} |\Delta t| \sum_{j=0}^n \|R^{n-j}\|_2, \\ &\leq \epsilon e^{2r\lambda_J} + \{\|h\|_{2,\infty}/|\Delta t|\} \int_0^r e^{2\lambda_J(r-s)} ds, \\ &= \epsilon e^{2r\lambda_J} \{\|h\|_{2,\infty}/|\Delta t|\} \{e^{2r\lambda_J} - 1\} / 2\lambda_J. \end{aligned} \quad (6.5)$$

As in the preceding Theorem, we may now use Lemma 2 to estimate  $\{\|h\|_{2,\infty}/|\Delta t|\}$  and obtain Eq. (6.3) from Eq.(6.5). QED.

It is instructive to compare the results in the well-posed case in Eq.(6.1), with the ill-posed results implied by Eq.(6.3). For this purpose, we must reevaluate Eq.(6.3) at the same  $t$  values that are used in Eq. (6.1). With  $\Delta t > 0$ ,  $t = k\Delta t$ , and  $\omega^k(x, y) = \omega(x, y, k\Delta t)$ , let  $\tilde{\omega}^k(x, y)$  now denote the previously computed backward solution evaluated at  $t = k\Delta t$ . With  $T = (N+1)\Delta t$ , let  $err^k(x, y) = \omega^k(x, y) - \tilde{\omega}^k(x, y)$ ,  $k = 0, 1, 2, \dots, N + 1$ , denote the error at  $t = k\Delta t$ . Again, choosing  $\gamma = (\lambda_J)^{1-p}$ , we get from Eq. (6.3),

$$\begin{aligned} \|err^k\|_2 &\leq (\lambda_J)^{-p} \{ \exp[2\lambda_J(T-t)] - 1 \} \|P\omega\|_{2,\infty} \\ &+ \epsilon \exp\{2\lambda_J(T-t)\} + O(\Delta t), \quad 0 \leq t \leq T. \end{aligned} \quad (6.6)$$

Here, the stabilization penalty is augmented by an additional term, resulting from amplification of the errors  $\kappa(x, y)$  in the given data at  $t = T$ , as indicated in Eq. (6.2). Both of the first two terms on the right in Eq. (6.6) grow monotonically as  $t \downarrow 0$ , reflecting backward in time marching from  $t = T$ .

Let the exact solution  $\omega(x, y, 0)$  at  $t = 0$ , satisfy a prescribed  $\mathcal{L}^2$  bound,

$$\|\omega^0\|_2 \leq M. \quad (6.7)$$

Again, with large  $T$ , and  $\lambda_J$  large enough to satisfy Eq. (5.5) in Lemma 1, the non-vanishing residuals in Eq. (6.6) lead to large errors, and the backward explicit scheme is not useful in that case. However, if  $T$  is small enough that

$$2\lambda_J T \leq \log(M/\epsilon), \quad (6.8)$$

with  $(\epsilon, M)$  as in Eqs. (6.2) and (6.7), we find, with  $t = k\Delta t$ , and  $\mu(t) = t/T$ ,

$$\begin{aligned} \|err^k\|_2 &\leq (\lambda_J)^{-p} \{ \exp[2\lambda_J(T-t)] - 1 \} \|P\omega\|_{2,\infty} \\ &\quad + M^{1-\mu(t)} \epsilon^{\mu(t)} + O(\Delta t), \quad 0 \leq t \leq T. \end{aligned} \quad (6.9)$$

The second term on the right in Eq. (6.9) represents the fundamental uncertainty in ill-posed backward continuation from noisy data, for solutions satisfying the prescribed bounds  $(\epsilon, M)$  in Eqs. (6.2) and (6.7). That uncertainty is known to be *best-possible* in the case of autonomous selfadjoint problems. Therefore, in a limited but potentially significant class of problems, the stabilized backward explicit scheme for the linearized problem in Eq. (5.1), can produce results differing from what is best-possible only by a small stabilization penalty as  $\Delta t \downarrow 0$ .

For example, with parameter values such as  $T = 10^{-3}$ ,  $M = 10^4$ ,  $\epsilon = 10^{-3}$ , we have  $M/\epsilon = 10^7 = \exp\{2\lambda_J T\}$ , and  $\lambda_J \geq 8059$ . Hence, with  $p = 3.0$ , we find  $(\lambda_J)^{-p} < 1.91 \times 10^{-12}$ . With  $t = k\Delta t$ , we would then obtain from Eq. (6.9),

$$\begin{aligned} \|err^k\|_2 &\leq M^{1-\mu(t)} \epsilon^{\mu(t)} \\ &\quad + (1.91 \times 10^{-5}) \|P\omega\|_{2,\infty} + O(\Delta t), \quad 0 \leq t \leq T, \end{aligned} \quad (6.10)$$

which may lead to an acceptable  $\mathcal{L}^2$  relative error  $(\|err^k\|_2 / \|\omega^k\|_2)$ .

**Remark.** In most applications of time-reversed problems, the values of  $M$  and  $\epsilon$  in Eq. (6.10), are seldom known accurately. In most cases, interactive adjustment of the parameter pair  $(\gamma, p)$  in Eqs. (4.6, 4.7), in the definition of the smoothing operator  $S$ , based on prior knowledge about the exact solution, is necessary to obtain useful reconstructions. This process is similar to the manual tuning of an FM station, or the manual focusing of binoculars, and likewise requires user recognition of a ‘correct’ solution. There may be several possible good solutions. Typical values of  $(\gamma, p)$  lie in the ranges  $10^{-12} \leq \gamma \leq 10^{-7}$ ,  $2.5 \leq p \leq 3.5$ .

### 7. Behavior in the nonlinear stabilized explicit scheme in Eq. (4.8).

It remains to be seen whether the linear analysis in Sections 5 and 6 is indicative of actual numerical behavior in the nonlinear system in Eq. (4.8). Four instructive backward recovery experiments will be presented and discussed. With the operator  $L^\dagger$  as in Eq (4.1), we now use second order accurate centered finite differencing for the space variables in the fully discrete non linear scheme

$$\tilde{\omega}^{n+1} = S\tilde{\omega}^n + \Delta t S(L^\dagger \tilde{\omega}^n), \quad \Delta \tilde{\psi}^{n+1} = -\tilde{\omega}^{n+1}. \quad (7.1)$$

Fast Fourier Transform (FFT) algorithms are used to synthesize the smoothing operator  $S$  defined in Eq. (4.7), and an efficient multigrid Poisson solver is used at every time step to solve  $\Delta\tilde{\psi}^{n+1} = -\tilde{\omega}^{n+1}$ .

All four experiments involve  $256 \times 256$  pixel gray scale images, defined by non-smooth underlying intensity data, with integer values ranging between zero and 255. These images have zero intensities on and near the boundary. In each case, the image intensity data are multiplied by 0.0025 to create the initial stream function  $\psi(x, y, 0)$ , with  $0 \leq \psi \leq 0.6375$ . The kinematic viscosity  $\nu = 0.01$  in all four cases, and  $U_{max}$ ,  $RE$ , are as defined in Eq. (2.2). The initial values for the forward problem,  $u(x, y, 0)$ ,  $v(x, y, 0)$ ,  $\omega(x, y, 0)$ , are obtained by numerical differentiation of  $\psi(x, y, 0)$ . All of these quantities are assumed defined on the unit square  $\Omega$ , and to vanish on  $\partial\Omega$  for the duration of the flow.

**USAF Resolution Chart.** This is illustrated in Figure 8.1, and documented in Table 1. The USAF Chart initial data are shown in the leftmost column of Figure 8.1 as the original sharp image, contour plots of the velocity component  $u(x, y, 0)$ , and contour plots of the vorticity  $\omega(x, y, 0)$ . We have  $U_{max} = 115$ ,  $RE = 11500$ , and  $\sup_{\Omega}\{|\omega(x, y, 0)|\} = 1.25 \times 10^5$ . With  $\Delta t = 1.0 \times 10^{-6}$ , the fully discrete scheme in Eq. (7.1) was solved forward in time for 1000 time steps to create the data at time  $T = 1.0 \times 10^{-3}$ , shown in the middle column of Figure 8.1. In this forward calculation, the operator  $S$  was chosen as the identity operator. No compensation was required, as the explicit scheme was found stable with such small  $\nu\Delta t$ .

Evidently, considerable change has occurred at time  $T = 1.0 \times 10^{-3}$ . Substantial erosion and disorganization of the sharp features in the leftmost column, is now apparent in the middle column of Figure 8.1. Moreover, as Table 1 indicates, the  $\mathcal{L}^2(\Omega)$  norms of the velocity components  $u$ ,  $v$ , are reduced to about 2/3 of their initial values, while the  $\mathcal{L}^2$  norm of the vorticity  $\omega$  is reduced to about 1/4 of its initial value.

The computed data at time  $T$  are affected by accumulated discretization and roundoff errors, exacerbated by repeated application of the elliptic solver. Using these data, and solving the fully discrete scheme in Eq. (7.1) backward in time for 1000 time steps, requires use of the smoothing operator  $S$ , with an appropriate choice of the parameters  $\gamma$  and  $p$ . Here, as is always the case in ill-posed reconstruction, *a priori knowledge* about the true solution is fundamental in arriving at useful values interactively. The explicit nature of the scheme in Eq. (7.1), together with its unconditional stability, allows for fast trial restorations using a relatively large time step  $|\Delta t|$ . Upon locating promising parameter values, a more refined search is undertaken with smaller  $|\Delta t|$ . With  $\gamma = 1.0 \times 10^{-12}$ ,  $p = 2.75$ , the stabilized explicit scheme produced the results shown in the rightmost column of Figure 8.1.

The recovery from the blurred data is surprisingly good. In Table 1, the restored values for the  $\mathcal{L}^2$  norms of  $u$ ,  $v$ ,  $\omega$ , are close to the original values. More significantly, the  $\mathcal{L}^2$  relative errors range from 12% to 14%.

Significantly less successful reconstruction would result from more severely blurred data at a value of  $T$  three to five times larger.

**Elizabeth Taylor.** Illustrated in Figure 8.2 and documented in Table 2, this experiment has  $T = 2.0 \times 10^{-3}$ ,  $U_{max} = 103$ ,  $RE = 10300$ , and  $\sup_{\Omega}\{|\omega(x, y, 0)|\} = 1.25 \times 10^5$ . As in Figure 8.1, the leftmost column contains the original sharp image, contour plots of the velocity component  $u(x, y, 0)$ , and contour plots of the vorticity  $\omega(x, y, 0)$ . With  $\Delta t = 1.0 \times 10^{-6}$ , the fully discrete scheme in Eq. (7.1) was

solved forward in time for 2000 time steps to create the data at time  $T$ , shown in the middle column of Figure 8.2. As in the preceding experiment,  $S$  was chosen as the identity operator. More erosion of the initial data is now apparent in the middle column in Figure 8.2, and Table 2 indicates that the  $\mathcal{L}^2$  norms of  $u$ ,  $v$ , have been reduced to 55% of their initial values, while the  $\mathcal{L}^2$  norm of  $\omega$  was reduced to less than 12% of its initial value. Nevertheless, very good recovery is still possible with  $\gamma = 1.0 \times 10^{-12}$ ,  $p = 2.75$ , leading to  $\mathcal{L}^2$  relative errors less than 5%. Larger values of  $T$  would lead to unsatisfactory reconstructions.

The previous two experiments used images of familiar objects, leading to easily grasped contour plots in Figures 8.1 and 8.2. The next two experiments involve images of complicated vortex flows actually found in nature. This results in the more complex contour plots shown in Figures 8.3 and 8.4.

**Kármán Vortex Street in clouds off Heard Island.** This is illustrated in Figure 8.3, and documented in Table 3. Here,  $U_{max} = 98$ ,  $RE = 9800$ , and  $\sup_{\Omega}\{|\omega(x, y, 0)|\} = 1.11 \times 10^5$ . With  $\Delta t = 1.0 \times 10^{-6}$ , and  $S$  the identity operator, the fully discrete scheme in Eq. (7.1) was solved forward in time for 2000 time steps to create the data at time  $T = 2.0 \times 10^{-3}$ , shown in the middle column of Figure 8.3. Evidently, dissipation has caused significant disorganization and erosion of sharp features, with the  $\mathcal{L}^2$  norms of  $u$ ,  $v$ , reduced to half their initial values, while the  $\mathcal{L}^2$  norm of  $\omega$  was reduced to less than 10% of its original value. Remarkably, the stabilized explicit scheme run backward with  $\gamma = 1.0 \times 10^{-12}$ ,  $p = 2.75$ , produced high quality reconstructions, with  $\mathcal{L}^2$  relative errors less than 6%. Significantly less accurate reconstructions would result from blurred data at larger values of  $T$ .

The original image in Figure 8.3 was taken by NASA's Aqua satellite on November 2 2015. Heard Island is located in the far south Indian Ocean, close to Antarctica.

**Twin Hurricanes over Hawaii.** Illustrated in Figure 8.4 and documented in Table 4, this experiment has  $T = 2.0 \times 10^{-3}$ ,  $U_{max} = 85$ ,  $RE = 8500$ , and  $\sup_{\Omega}\{|\omega(x, y, 0)|\} = 1.14 \times 10^5$ . As in the previous experiment, the leftmost column contains the original sharp image, contour plots of the velocity component  $u(x, y, 0)$ , and contour plots of the vorticity  $\omega(x, y, 0)$ . With  $S$  the identity operator, and  $\Delta t = 1.0 \times 10^{-6}$ , the fully discrete scheme in Eq. (7.1) was solved forward in time for 2000 time steps to create the data at time  $T$ , shown in the middle column of Figure 8.4. As before, there is considerable dissipation and substantial erosion of sharp features, with the  $\mathcal{L}^2$  norms of  $u$ ,  $v$ , reduced to 38% of their initial values, while the  $\mathcal{L}^2$  norm of  $\omega$  was reduced to less than 7% of its initial value. Again, successful reconstruction of  $u(x, y, 0)$ ,  $v(x, y, 0)$ ,  $\omega(x, y, 0)$ , was found possible with  $\gamma = 1.0 \times 10^{-12}$ ,  $p = 2.75$ , in the stabilized explicit scheme in Eq. (7.1). Here, the  $\mathcal{L}^2$  relative errors were less than 4%. At larger values of  $T$ , the blurring is too severe to permit useful recovery.

The original image in Figure 8.4 was obtained by NASA on August 31 2016, using the Suomi National Polar Orbiting Weather Satellite.

**Reconstructions with additional noise.** In each of the above experiments, the stream functions  $\psi(x, y, T)$ , computed using the forward Navier-Stokes equations,

contain an appreciable amount of noise originating from accumulated discretization and roundoff errors. Such stream functions generated the data  $u$ ,  $v$ ,  $\omega$  at time  $T$  that were used as input in the backward problem, and that are shown in the middle columns in Figures 8.1–8.4. However, further experiments were conducted with  $\psi(x, y, T)$  replaced by  $\psi^\dagger(x, y, T) \equiv \psi(x, y, T) + 0.02 \phi(x, y, T)$ , where  $\phi(x, y, T)$  is the forward computed Navier-Stokes stream function associated with a different image. Quality reconstructions were still obtained with such noisier input data  $\psi^\dagger(x, y, T)$ , albeit with larger  $\mathcal{L}^2$  relative errors than are reported in Tables 1–4.

**8. Concluding remarks.** To the author’s knowledge, work on numerical algorithms for solving Navier-Stokes equations backward in time, has not previously appeared in the research literature. The primary aim in this paper was to open doors, and demonstrate the possibility of useful reconstruction in a class of problems generally considered intractable. Given the discussion in Section 3 following the results in Eqs. (3.12, 3.13), and the fact that  $U_{max} \geq 85$ ,  $\sup_{\Omega} \{|\omega(x, y, 0)|\} \geq 1.0 \times 10^5$ , in all four experiments in Section 7, the successful recoveries in each of these experiments from data at  $T \geq 1.0 \times 10^{-3}$ , were quite unexpected. Moreover, high quality reconstruction from similar  $T$  values was found possible in numerous other images.

# BACKWARD NAVIER-STOKES ON USAF CHART

MAX SPEED = 115, RE= 11500, T= 1.0E-3

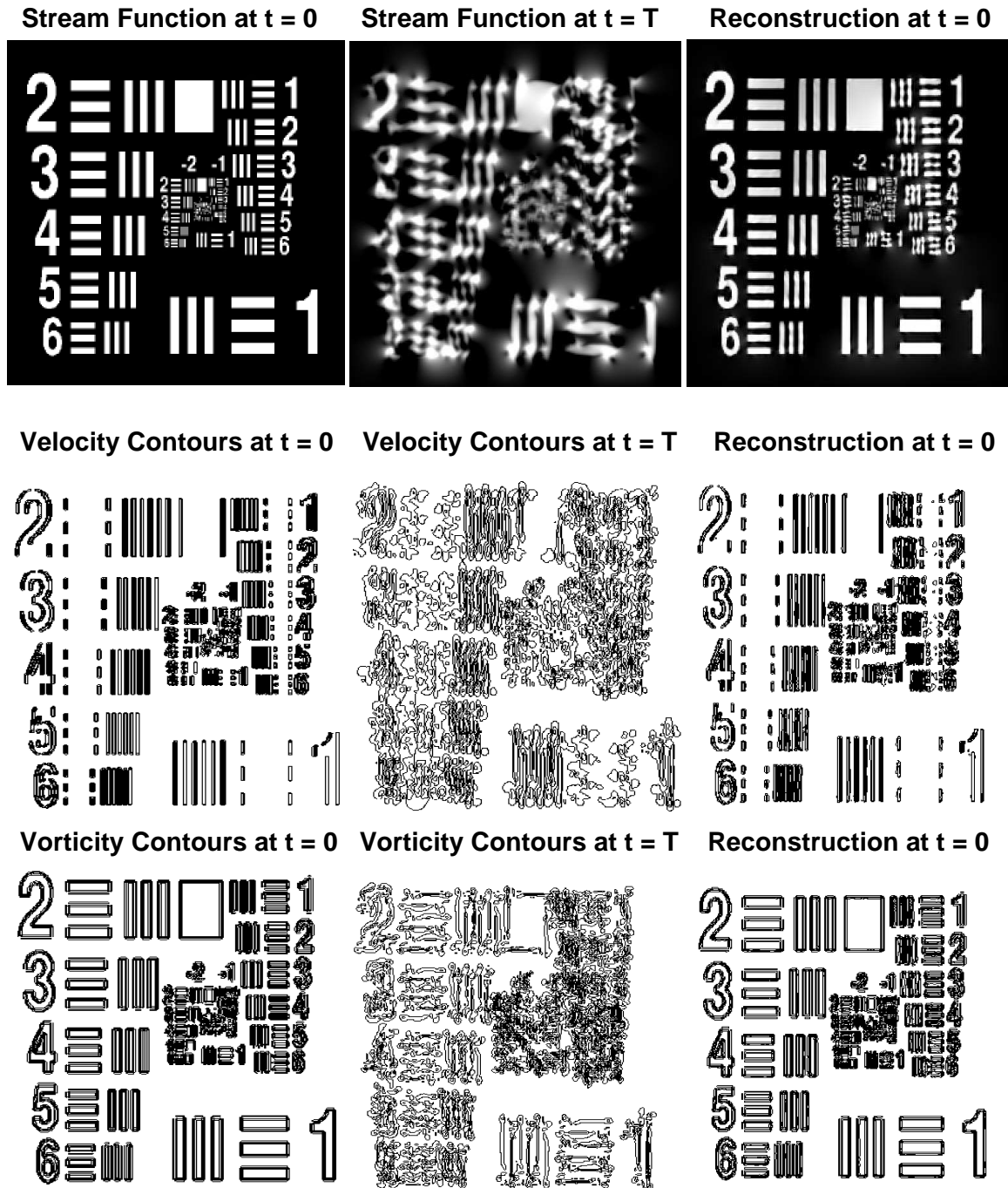


FIG. 8.1. Backward recovery in USAF Resolution Chart image, with  $\nu = 0.01$ ,  $U_{max} = 115$ ,  $RE = 11500$ ,  $\sup_{\Omega}\{|\omega(x, y, 0)|\} = 1.25 \times 10^5$ ,  $T = 1.0 \times 10^{-3}$ . Using data shown in middle column, stabilized explicit scheme seeks to reconstruct initial data shown in leftmost column. Actually recovered data, shown in rightmost column, are documented in Table 1.

## BACKWARD NAVIER-STOKES ON LIZ TAYLOR

MAX SPEED = 103, RE= 10300, T= 2.0E-3

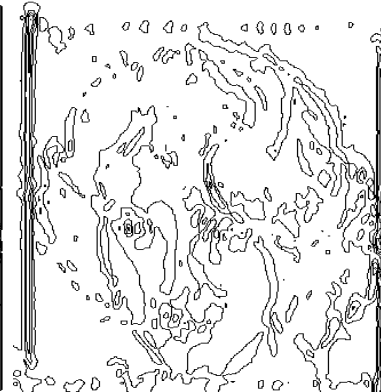
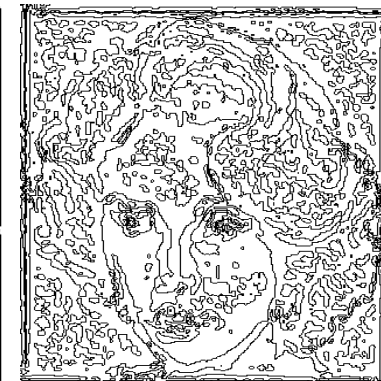
Stream Function at  $t = 0$ Stream Function at  $t = T$ Reconstruction at  $t = 0$ Velocity Contours at  $t = 0$ Velocity Contours at  $t = T$ Reconstruction at  $t = 0$ Vorticity Contours at  $t = 0$ Vorticity Contours at  $t = T$ Reconstruction at  $t = 0$ 

FIG. 8.2. Backward recovery in Elizabeth Taylor image, with  $\nu = 0.01$ ,  $U_{max} = 103$ ,  $RE = 10300$ ,  $\sup_{\Omega} \{|\omega(x, y, 0)|\} = 1.25 \times 10^5$ ,  $T = 2.0 \times 10^{-3}$ . Using data shown in middle column, stabilized explicit scheme seeks to reconstruct initial data shown in leftmost column. Actually recovered data, shown in rightmost column, are documented in Table 2.

# BACKWARD NAVIER–STOKES ON VORTEX STREET

MAX SPEED = 98, RE= 9800, T= 2.0E–3

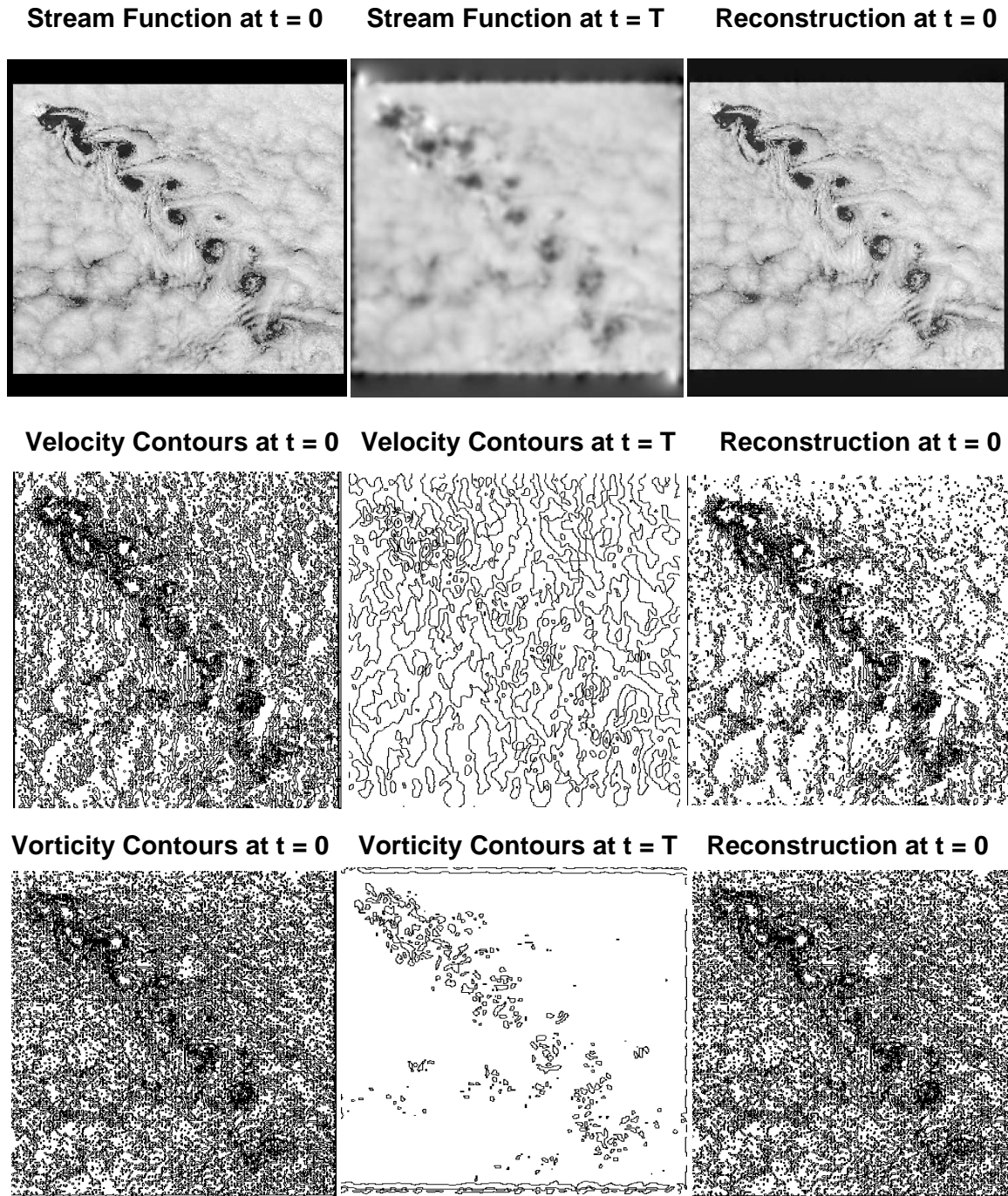


FIG. 8.3. Backward recovery in November 2 2015 NASA Aqua satellite image of Kármán Vortex Street in clouds off Heard Island. Here,  $\nu = 0.01$ ,  $U_{max} = 98$ ,  $RE = 9800$ ,  $\sup_{\Omega}\{|\omega(x,y,0)|\} = 1.11 \times 10^5$ ,  $T = 2.0 \times 10^{-3}$ . Using data shown in middle column, stabilized explicit scheme seeks to reconstruct initial data shown in leftmost column. Actually recovered data, shown in rightmost column, are documented in Table 3.

# BACKWARD NAVIER-STOKES ON TWO HURRICANES

MAX SPEED = 85, RE= 8500, T= 2.0E-3

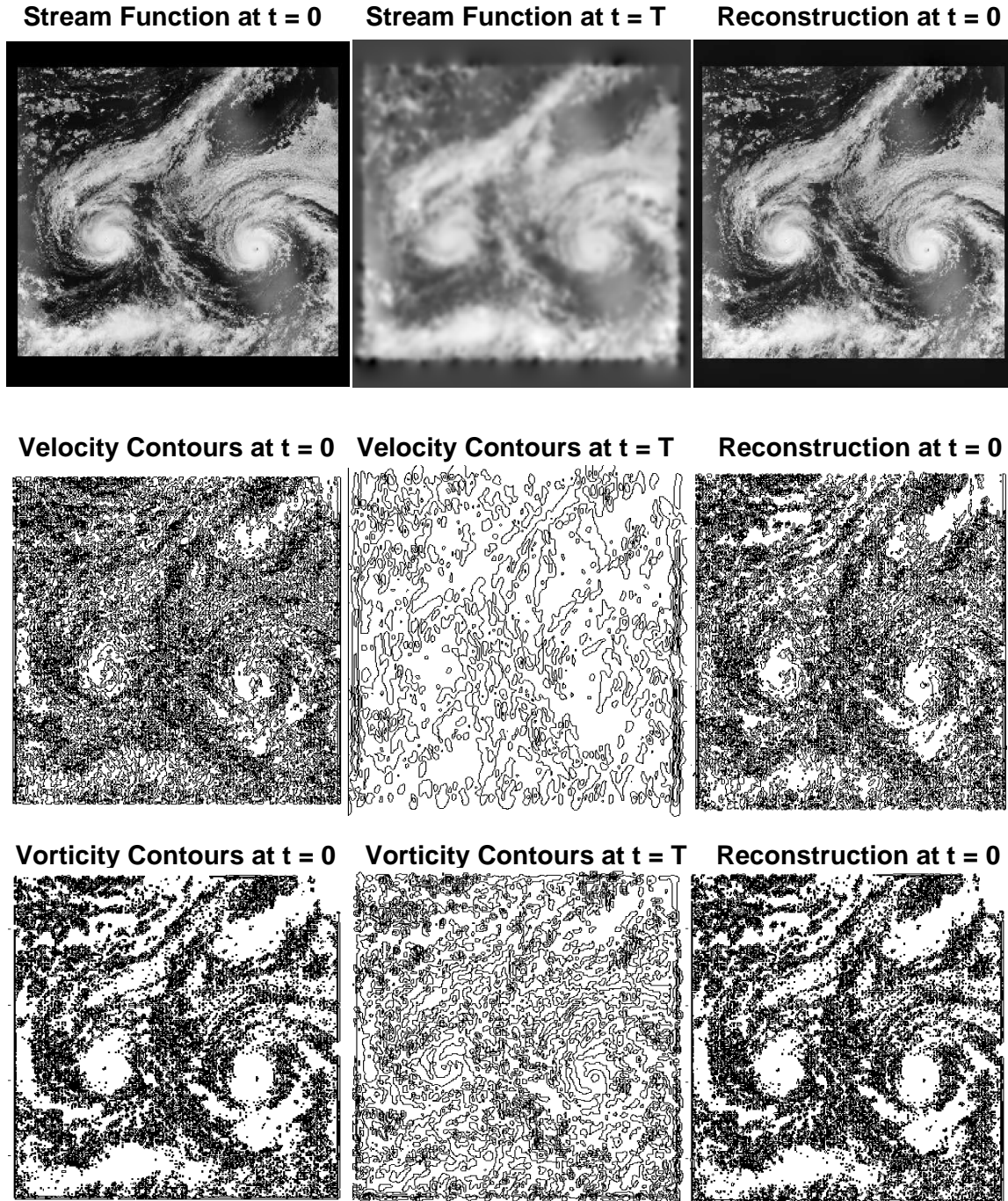


FIG. 8.4. Backward recovery in August 31 2016 NASA Suomi weather satellite image of twin hurricanes Madeline and Lester over Hawaii. Here,  $\nu = 0.01$ ,  $U_{max} = 85$ ,  $RE = 8500$ ,  $\sup_{\Omega}\{|\omega(x, y, 0)|\} = 1.14 \times 10^5$ ,  $T = 2.0 \times 10^{-3}$ . Using data shown in middle column, stabilized explicit scheme seeks to reconstruct initial data shown in leftmost column. Actually recovered data, shown in rightmost column, are documented in Table 4.

TABLE 1  
*USAF Chart image at RE=11500*  
 $\mathcal{L}^2(\Omega)$ -norm behavior in backward recovery from data at  $T = 1 \times 10^{-3}$

Variable	$\mathcal{L}^2$ norm at 0	$\mathcal{L}^2$ norm at $T$	Recovered at 0	$\mathcal{L}^2$ rel err at 0
$u = \psi_y$	23.6	14.6	23.6	11.9 %
$v = -\psi_x$	21.2	14.0	21.2	13.1 %
$\omega = -\Delta\psi$	15882	4009	15774	13.9%

TABLE 2  
*Elizabeth Taylor image at RE=10300*  
 $\mathcal{L}^2(\Omega)$ -norm behavior in backward recovery from data at  $T = 2 \times 10^{-3}$

Variable	$\mathcal{L}^2$ norm at 0	$\mathcal{L}^2$ norm at $T$	Recovered at 0	$\mathcal{L}^2$ rel err at 0
$u = \psi_y$	9.6	5.3	9.5	3.3 %
$v = -\psi_x$	9.5	5.3	9.4	3.3 %
$\omega = -\Delta\psi$	7806	895	7694	4.7 %

TABLE 3  
*Kármán Vortex Street image at RE=9800*  
 $\mathcal{L}^2(\Omega)$ -norm behavior in backward recovery from data at  $T = 2 \times 10^{-3}$

Variable	$\mathcal{L}^2$ norm at 0	$\mathcal{L}^2$ norm at $T$	Recovered at 0	$\mathcal{L}^2$ rel err at 0
$u = \psi_y$	10.6	5.2	10.5	4.4 %
$v = -\psi_x$	11.5	5.5	11.4	4.3 %
$\omega = -\Delta\psi$	10668	1005	10522	5.8 %

TABLE 4  
*Twin Hurricanes image at RE=8500*  
 $\mathcal{L}^2(\Omega)$ -norm behavior in backward recovery from data at  $T = 2 \times 10^{-3}$

Variable	$\mathcal{L}^2$ norm at 0	$\mathcal{L}^2$ norm at $T$	Recovered at 0	$\mathcal{L}^2$ rel err at 0
$u = \psi_y$	12.3	4.7	12.1	3.7 %
$v = -\psi_x$	12.7	4.8	12.6	3.6 %
$\omega = -\Delta\psi$	14301	965	14093	3.9 %

## REFERENCES

- [1] Atmadja J, Bagtzoglou AC. State of the art report on mathematical methods for groundwater pollution source identification. *Environ. Forensics* 2001;2:205-214.
- [2] Bagtzoglou AC, Atmadja J. The marching-jury backward beam equation and quasi-reversibility methods for hydrologic inversion: Application to contaminant plume spatial distribution recovery. *Water Resour. Res.* 2003; 39:1038, doi:10.1029/2001WR001021, 2003.
- [3] Bagtzoglou AC, Kenney ED, Hiscox A, et al. Optimization-based atmospheric plume source identification. *Environ. Forensics* 2014;15:147–158.
- [4] Ismail-Zadeh A, Schubert G, Tsepelev I, et al. Inverse problem of thermal convection: numerical approach and application to mantle plume restoration. *Phys Earth Planet Inter.* 2004;145:99-114.
- [5] Ismail-Zadeh A, Korotkii A, Schubert G, et al. Numerical techniques for solving the inverse retrospective problem of thermal evolution of the Earth interior. *Comput Struct* 2009;87:802–811.
- [6] Carasso AS, Bright DS, Vladár AE. APEX method and real-time blind deconvolution of scanning electron microscope imagery. *Opt Eng* 2002;41:2499–2514.
- [7] Carasso AS. APEX blind deconvolution of color Hubble space telescope imagery and other astronomical data. *Opt Eng* 2006;45:107004.
- [8] Carasso AS. Bochner subordination, logarithmic diffusion equations, and blind deconvolution of Hubble space telescope imagery and other scientific data. *SIAM J Imaging Sci* 2010;3:954–980.
- [9] Ou K, Jameson A. Unsteady adjoint method for the optimal control of advection and Burgers' equation using high order spectral difference method. 49th AIAA Aerospace Science Meeting, 4-7 January 2011. Orlando, Florida.
- [10] Allahverdi N, Pozo A, Zuazua E. Numerical aspects of large-time optimal control of Burgers' equation. *ESAIM Mathematical Modeling and Numerical Analysis* 2016;50:1371–1401.
- [11] Gosse L, Zuazua E. Filtered gradient algorithms for inverse design problems of one-dimensional Burgers' equation. In: Gosse L, Natalini R, editors. *Innovative algorithms and analysis. SINDAM Series.* Springer; 2017. p. 197227.
- [12] Lundvall J, Kozlov V, Weinerfelt P. Iterative methods for data assimilation for Burgers' equation. *J. Inv. Ill-Posed Problems.* 2006;14:505–535.
- [13] Auroux D, Bansart P, Blum J. An evolution of the back and forth nudging for geophysical data assimilation: application to Burgers' equation and comparison. *Inverse Probl. Sci. Eng.* 2013;21:399–419.
- [14] Carasso AS. Compensating operators and stable backward in time marching in nonlinear parabolic equations. *Int J Geomath* 2014;5:1–16.
- [15] Carasso AS. Stable explicit time-marching in well-posed or ill-posed nonlinear parabolic equations. *Inverse Probl. Sci. Eng.* 2016;24:1364–1384.
- [16] Carasso AS. Stable explicit marching scheme in ill-posed time-reversed viscous wave equations. *Inverse Probl. Sci. Eng.* 2016;24:1454–1474.
- [17] Carasso AS. Stabilized Richardson leapfrog scheme in explicit stepwise computation of forward or backward nonlinear parabolic equations. *Inverse Probl. Sci. Eng.* 2017;25:1–24.
- [18] Carasso AS. Stabilized backward in time explicit marching schemes in the numerical computation of ill-posed time-reversed hyperbolic/parabolic systems. *Inverse Probl. Sci. Eng.* 2018;1:132. DOI:10.1080/17415977.2018.1446952
- [19] Carasso AS. Stable explicit stepwise marching scheme in ill- posed time-reversed 2D Burgers' equation. *Inverse Probl. Sci. Eng.* 2018; DOI:10.1080/17415977.2018.1523905
- [20] Johnston H, Liu JG. Finite difference schemes for incompressible flow based on local pressure boundary conditions. *J. Comput. Phys.* 2002;180:120–154.
- [21] Ghadimi P, Dashtimanesh A. Solution of 2D Navier-Stokes equation by coupled finite difference-dual reciprocity boundary element method. *Applied Mathematical Modelling* 2011;35:2110–2121.
- [22] Hou TM, Stable fourth-order stream function methods for incompressible flows with boundaries. *Journal of Computational Mathematics* 2009;27:411–458.
- [23] Zhu H, Shu H, Ding M. Numerical solutions of two-dimensional Burgers equations by discrete Adomian decomposition method. *Computers and Mathematics with Applications* 2010;60:840848.

- [24] Wang Y, Navon IM, Wang X, Cheng Y. 2D Burgers equation with large Reynolds number using POD/DEIM and calibration. *Int. J. Numer. Meth. Fluids* 2016;82:909931.
- [25] Dehghan M. Finite difference procedures for solving a problem arising in modeling and design of certain optoelectronic devices. *Mathematics and Computers in Simulation* 2006;71:16–30.
- [26] Dehghan M, Abbaszadeh M. Proper orthogonal decomposition variational multiscale element free Galerkin (POD-VMEFG) meshless method for solving incompressible Navier-Stokes equation. *Computer Methods in Applied Mechanics and Engineering* 2016;311:856–888.
- [27] Dehghan M, Abbaszadeh M. An upwind local radial basis functions-differential quadrature (RBF-DQ) method with proper orthogonal decomposition (POD) approach for solving compressible Euler equation. *Engineering Analysis with Boundary Elements* 2018;92:244–256.
- [28] Sedaghatjoo Z, Dehghan M, Hosseinzadeh H. Numerical solution of 2D Navier-Stokes equation discretized via boundary elements method and finite difference approximation. *Engineering Analysis with Boundary Elements* 2018;96:64–77.
- [29] Serrin J, The initial value problem for the Navier-Stokes equations. *Proceedings of Symposium on Non-Linear Problems*, pp. 69-98. University of Wisconsin Press; 1963.
- [30] Ames KA, Straughan B. *Non-Standard and Improperly Posed Problems*. New York (NY): Academic Press; 1997.
- [31] Knops RJ. Logarithmic convexity and other techniques applied to problems in continuum mechanics. In: Knops RJ, editor. *Symposium on non-well-posed problems and logarithmic convexity*. Vol. 316, *Lecture notes in mathematics*. New York (NY): Springer-Verlag; 1973.
- [32] Knops RJ, Payne LE. On the stability of solutions of the Navier-Stokes equations backward in time. *Arch. Rat. Mech. Anal.* 1968;29:331–335.
- [33] Payne LE. Uniqueness and continuous dependence criteria for the Navier-Stokes equations. *Rocky Mountain J. Math.* 1971;2:641–660.
- [34] Payne LE, Straughan B. Comparison of viscous flow backward in time with small data. *Int. J. Nonlinear Mech.* 1989;24:209–214.
- [35] Payne LE. Some remarks on ill-posed problems for viscous fluids. *Int. J. Engng Sci.* 1992;30:1341–1347.
- [36] Carasso AS. Reconstructing the past from imprecise knowledge of the present: Effective non-uniqueness in solving parabolic equations backward in time. *Math. Methods Appl. Sci.* 2012;36:249-261.
- [37] Carasso A. Computing small solutions of Burgers' equation backwards in time. *J. Math. Anal. App.* 1977;59:169–209.
- [38] Hào DN, Nguyen VD, Nguyen VT. Stability estimates for Burgers-type equations backward in time. *J. Inverse Ill Posed Probl.* 2015;23:41–49.
- [39] Richtmyer RD, Morton KW. *Difference Methods for Initial Value Problems*. 2nd ed. New York (NY): Wiley; 1967.